Processing outcomes of atomic force microscope tip-based nanomilling with different trajectories on single-crystal silicon

Jiqiang Wang[1,2], Yongda Yan[1,2], Zihan Li[2], Yanquan Geng[1,2,*], Xichun Luo[3], Pengfei Fan[3]

[1] *Key Laboratory of Micro-systems and Micro-structures Manufacturing of Ministry of Education, Harbin Institute of Technology, Harbin, Heilongjiang 150001, P.R. China*

[2] *Center for Precision Engineering, Harbin Institute of Technology, Harbin, Heilongjiang 150001, P.R. China*

[3]*Centre for Precision Manufacturing, Department of Design, Manufacture and Engineering Management, University of Strathclyde, Glasgow, UK.*

* *Corresponding author. Tel.: +86-0451-86412924. Fax: +86-0451-86415244*

E-mail address: gengyanquan@hit.edu.cn (Y. Q. Geng)

Abstract

Atomic force microscope (AFM) tip-based nanomilling is an emerging technology for machining nanostructures with a high rate of material removal and slight tip wear. However, subsurface damage induced by nanomilling is poorly understood. In this study, we investigated nanomilling-induced subsurface damage of single-crystal silicon experimentally and with molecular dynamics simulations. We studied the effect of clockwise and anticlockwise trajectories on the nanochannel morphology. The clockwise trajectory resulted in a ‘U’-shaped nanochannel at a relatively low normal load. Transmission electron microscopy and Raman spectroscopy analysis of the nanochannel subsurface revealed atomic-scale defects,

including dislocations, stacking faults, and amorphous silicon. Molecular dynamics simulations described the evolution of the phase transformation and subsurface damage. This work reveals the mechanism of subsurface damage of single-crystal silicon in nanomilling, which will facilitate the machining of nanostructures with minimal subsurface damage.

Keywords: Atomic force microscope, nanomilling, single-crystal silicon, subsurface damage, phase transformation

1. Introduction

Single-crystal silicon is one of the most important semiconductors in the semiconductor industry, and is used in applications such as micro-electronics, photovoltaic solar panels, micro-electro-mechanical systems (MEMS), and micro- and nanofluidic fields [1-3]. Nanostructures, such as nanochannels, fabricated on single-crystal silicon using mechanical machining are fundamental for such applications. However, because of tool–workpiece contact in the machining process, subsurface damage invariably occurs just beneath the workpiece surface [4,5], which affects the mechanical, electronic, and optical performance of silicon devices. Another key determinant of performance is the surface integrity of the machined nanostructure. Thus, it is important to study the subsurface damage and surface integrity of nanostructures fabricated by mechanical machining.

Ultra-precision machining approaches, including single-point diamond turning (SPDT), polishing, and grinding, are commonly used to machine single-crystal silicon

in the ductile regime [6-9]. However, it is difficult to machine a nanostructure using SPDT to below 100 nm because of the kinematic accuracy of the rigid machining system. Machining systems for grinding and polishing are more flexible than those of SPDT, making it easy to obtain a surface with higher surface integrity. However, there are several drawbacks of these methods, including low machining efficiency, unpredictable machined depth, and their inability to form single nanostructures (such as nanochannels). Atomic force microscope (AFM) tip-based direct mechanical nanoscratching is a powerful approach to machine nanostructures. This approach has many merits, such as ease of use, low requirements for the processing environment, and high machining flexibility [10-12]. The dimensions — especially the machined depth of the nanostructures — can be predicted precisely by considering the machining parameters and material properties of the specimen [13]. Furthermore, it is easy to machine nanochannels with this machining system. Nevertheless, for the tip-based single-scratch method, the channel shape can only be determined by the tip geometry and the material removal rate needs to be improved.

The AFM tip-based nanomilling method was proposed to overcome the aforementioned drawbacks of the single-scratch nanofabrication approach. The ratio of the depth to width of the channel can be controlled by the driving voltage of the piezoelectric actuator and the normal load. Moreover, the material removal rate at large machined depths is much greater than that of the single-scratch method for the same applied normal load [14]. The nanomilling approach has been used to fabricate nanostructures on polymers, metals, and photoresists [15-17]. However, for brittle

materials, such as single-crystal silicon, mechanical machining inevitably induces damage and microstructural change of the sample under the machined surface [18]. In our previous study, we investigated the mechanism of nanomilling and subsurface damage caused by a non-circular nanomilling trajectory [19]. However, the effect of clockwise and anticlockwise nanomilling trajectories on the machining outcomes such as the shape of the nanochannel and the formation process of chips were not studied. Furthermore, the subsurface damage caused by a circular nanomilling trajectory was not investigated. Thus, the aforementioned concerns should be further explored. Molecular dynamics (MD) simulations are effective for studying the nanomachining process, and can even reveal the dynamic evolution process of the generated atomic defects [20]. Nevertheless, to our knowledge, MD simulations for nanomilling on single-crystal silicon have been not reported.

The objective of the present study was to understand the effect of clockwise and anticlockwise tip-based nanomilling on the subsurface damage and morphology of nanochannels fabricated on single-crystal silicon. Furthermore, we compared the material removal rate for machining using nanomilling and the single -scratch method. Raman spectroscopy and TEM were used to study the subsurface structure of the nanostructures machined using nanomilling with a circular trajectory. The dynamic evolution of the subsurface damage and morphology were further studied using MD simulations. The obtained results can be used to understand the morphology of machined nanostructures and the subsurface damage mechanism caused by nanomilling.

2. Experimental details

2.1 AFM-based nanomilling set-up and methods

As shown in Fig. 1(a), an AFM tip-based nanomilling set-up consisted of a piezoelectric actuator (P-122.01, PI Company, Germany) and a commercial AFM system (Dimension Icon, Bruker, Karlsruhe, Germany). The two-dimensional piezoelectric actuator was driven by a sinusoidal signal and moved in the horizontal plane. To obtain the driving sinusoid signals, a commercial signal generator (AFG1022, Tektronix, USA) and signal amplifier (PZD350A, TREK, USA) were used. The maximum travel ranges in both the x and y directions for the piezoelectric actuator were 1 μm. The specimen was fixed on the piezoelectric actuator. A revolving translational movement of the specimen could be obtained when the piezoelectric actuator was driven by a sinusoid signal with 90° phase difference in x- and y-directions. Thus, as illustrated in Fig. 1(b), the nanomilling process was achieved with the aid of the relative movement between the tip and specimen. Figure 1(c) shows a scanning electron microscopy (SEM) image of the triangular pyramidal diamond tip (PDNISP, Bruker, Germany) used in this study. The tip cantilever was made of stainless steel with a normal spring constant (K_N) of 286 N/m provided by the manufacturer. The front angle (θ_f), back angle (θ_b), and side angle (θ_s) of the tip, as illustrated in Fig. 1(d) and (e), were 55°, 35°, and 51°, respectively. The specimen was a single-side-polished single-crystal silicon (100) wafer, which was purchased from Suzhou Research Semiconductor Co., Ltd., China. The surface root-mean-square roughness of the specimen was measured to be about 0.1 nm by scanning a 1 μm ×

1 μm area using the AFM. Five normal loads in the range of 60–180 μN with steps of 30 μN (Fig. 1(a)) were used to perform the machining process; the load was constant during nanomilling. Furthermore, the driving voltage and frequency (f) of the sinusoidal signals in both the x and y directions were 125 V and 500 Hz, respectively. The driving amplitude (A) of the piezoelectric actuator was measured to be 370 nm. Thus, the linear velocity of the tip can be obtained by $V=\pi fA$, which is calculated to be 580 μm/s. The feed direction of the tip was selected as side-forward and the nanomilling process was along the in-plane Si $[\bar{1}\bar{1}0]$ orientation.

SEM (Quanta 200FEG, FEI, USA) and AFM (Dimension Icon, Bruker, Karlsruhe, Germany) were used to investigate the morphologies of the nanochannels. The obtained nanochannels were analyzed immediately using SEM and were then ultrasonically cleaned in alcohol solution for approximately 10 minutes to remove the generated chips. The AFM measurements were performed using a new silicon tip (radius of 10 nm, TESPA, Bruker, Germany) in tapping mode. The phase structure of the machined nanochannels and subsurface characteristics were investigated using a commercial Renishaw Raman system (InVia-Reflex, Renishaw, UK) and TEM (FEI Tecnai F20, USA), respectively. The laser wavelength of the Raman system was 633 nm and the power of the laser beam was 1.7 mW. A 100× objective lens was selected such that the spot of the laser was approximately 0.8 μm. A focused-ion-beam (FIB, FEI Helios NanolabG3 UC, USA) system was used to prepare the cross-sectional TEM samples. The TEM samples were cut perpendicularly to the nanochannels. To enable electron transmission, the samples were thinned to approximately 90 nm using

the FIB technique.

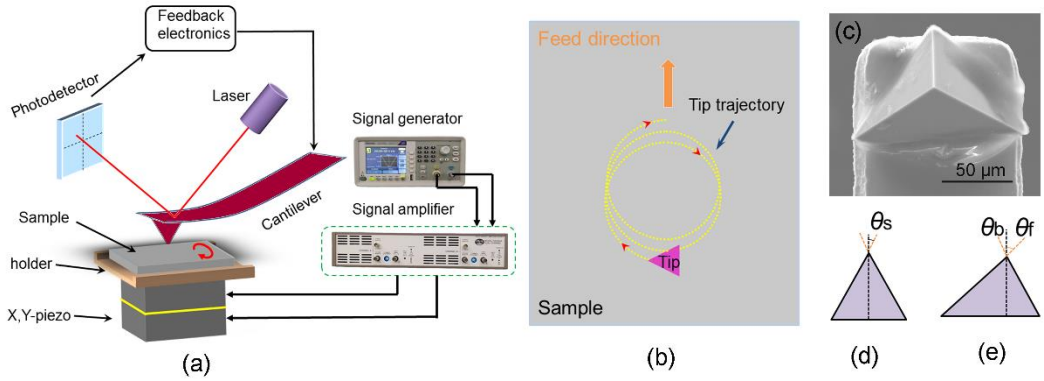

Fig. 1. (a) Schematic diagram of the tip-based nanomilling set-up. (b) Schematic diagram of the nanomilling process. (c–e) SEM micrograph and schematic diagrams of the side and front views of the diamond AFM tip.

2.2 MD simulation model

A three-dimensional (3D) MD nanomilling model was constructed as shown in Fig. 2. The model consisted of a rigid diamond tool and a single-crystal silicon workpiece. The size of the crystal silicon workpiece was 59 nm × 37 nm × 28 nm, and the crystal orientations for *x*, *y*, and *z* direction were [110], [$\bar{1}$10], and [002], respectively. The silicon atoms were categorized as either Newtonian or boundary atoms. The boundary atoms were used to reduce the boundary effect and to maintain the proper symmetry of the lattice. To reduce the effect of simulation scale, periodic boundaries were applied in the *x* and *y* directions. Nanomilling was simulated on the (100) surface along the [$\bar{1}\bar{1}$0] direction of the single-crystal-silicon workpiece. The analytical bond order potential (ABOP), which is an appropriate potential for simulating covalently bonding materials [21], was used to calculate the interatomic forces between Si atoms. The interaction between tip-workpiece (C–Si) atoms was expressed as the Morse potential [22]. The simulation model was equilibrated to 300

7

K under the canonical (NVT) ensemble in 50 ps, and the initial velocities of the workpiece atoms were assigned in accordance with the Maxwell–Boltzmann distribution. The tip was pressed into the workpiece under a normal load of 3.4 μN and moved with a feed rate of 80 m/s. Furthermore, for tip rotation, the maximum displacement in the *x* and *y* directions was 0.4 nm. The moving period was 10 ps. The other simulation parameters are listed in Table 1. The MD simulation was performed with the software Large-scale Atomic/Molecular Massively Parallel Simulator (LAMMPS) [23]. The software OVITO was used to visualize the simulation results [24].

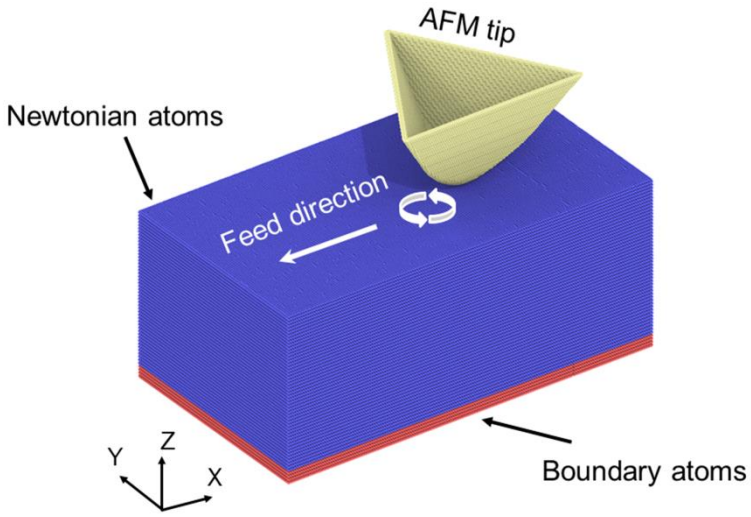

Fig. 2. Three-dimensional MD simulation model.

Table 1 MD simulation parameters

Parameters	Value
Workpiece size	58 nm×37 nm×28 nm
Atoms in workpiece	3035857
Atoms in Tool	106614
Feed velocity	80 m/s
Machining distance	26 nm
Tip rotation period	10 ps

8

3. Results and discussion

3.1 Nanochannel morphology

The effect of different tip trajectories (i.e. single-scratch, anticlockwise, and clockwise) on the nanochannel morphology was investigated using SEM and AFM. Figure 3(a) shows the AFM image and corresponding cross-section of the nanochannel fabricated using the single-scratch approach with a normal load of 180 μN. The inset is an SEM image of the nanochannel. In the AFM image, there are no pile-ups on either side of the channel. The cross-section of the nanochannel displays a 'V' shape, which depends on the shape of the tip. In the SEM image, several small chips can be observed.

Figure 3(b) shows the AFM image of the nanochannel machined using an anticlockwise trajectory with a normal load of 60 μN. The tip trajectory and feed direction are marked in the AFM image. This image reveals the generation of pile-ups during nanomilling, which were distributed on the left side of the tip feed direction. Moreover, chips can also be found in the SEM image of the channel (inset in the right panel). The cross-section corresponding to the nanochannel has a 'V' shape that is much wider than that of the nanochannel machined with a single scratch. Figure 3(c) and (d) show the AFM images of the nanochannels machined using a clockwise trajectory with normal loads of 60 and 180 μN, respectively. In this case, the chips were distributed on the right side and pile-ups were generated on the left side of the tip feed direction. The inset SEM images also reveal the generation of pile-ups and chips. The width of the 'V'-shaped cross-section of the nanochannel machined with a

normal load of 180 μN (Fig. 3(d)) was similar to that obtained with an anticlockwise trajectory at the same load (Fig. 3(b)). By contrast, the cross-section of the nanochannel fabricated with a normal load of 60 μN had a 'U' shape. From the different cross-sections of the nanochannels, we estimate that the volume of material removal for clockwise nanomilling was approximately 10 times greater than that for the single-scratch approach for a normal load of 180 μN. Thus, our results show that the rate of material removal is substantially improved using this nanomilling approach.

10

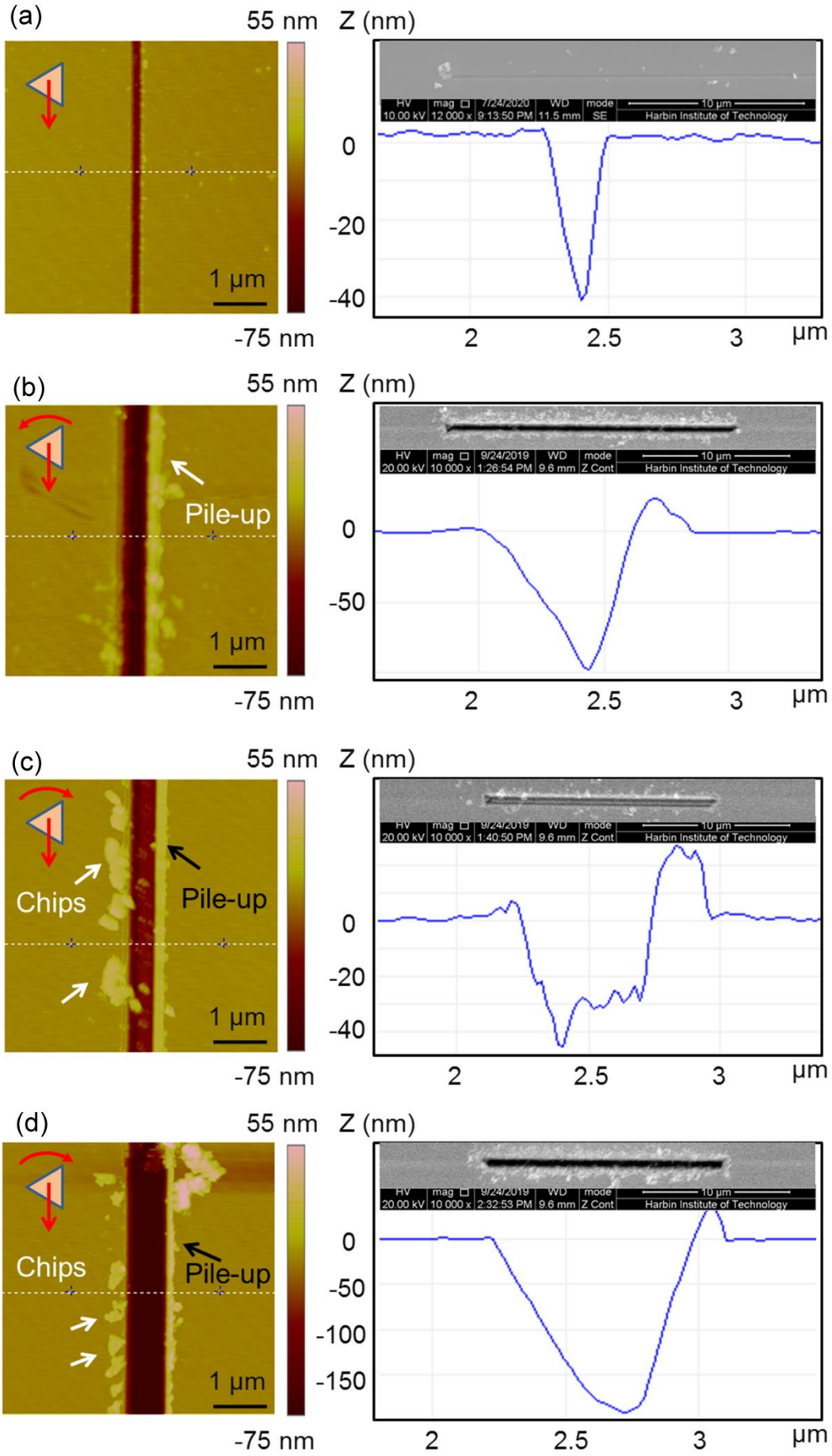
(a)
55 nm
Z (nm)
1 μm
-75 nm
0
-20
-40
2
2.5
3
μm
(b)
55 nm
Z (nm)
Pile-up
1 μm
-75 nm
0
-50
2
2.5
3
μm
(c)
55 nm
Z (nm)
Chips
Pile-up
1 μm
-75 nm
0
-20
-40
2
2.5
3
μm
(d)
55 nm
Z (nm)
Chips
Pile-up
1 μm
-75 nm
0
-50
-100
-150
2
2.5
3
μm

Fig. 3. (a–d) Typical AFM images and corresponding cross-sections of the nanochannels fabricated with a single-scratch, an anticlockwise trajectory, a clockwise trajectory with a load of 60 μN, and a clockwise trajectory with a load of 180 μN, respectively.

Figure. 4(a) illustrates the relationship between the machined depth and the applied normal load when machining using the single-scratch approach, which indicates the depth of the nanochannel is almost linearly proportional to the applied normal load. Figure 4(b) shows that the machined depth increased with increasing applied normal load for both the anticlockwise and clockwise trajectories. The machined depths were smaller with the clockwise trajectory than with the anticlockwise trajectory for normal loads lower than 150 μN. The morphology of the nanochannels fabricated using anticlockwise trajectory always had a 'V' shape. However, for nanochannels machined using the clockwise trajectory, there was a critical normal load that determined whether the channel had a 'V' or 'U' shape. These nanochannels were 'U'-shaped for normal loads smaller than 150 μN and 'V'-shaped for loads larger than 150 μN.

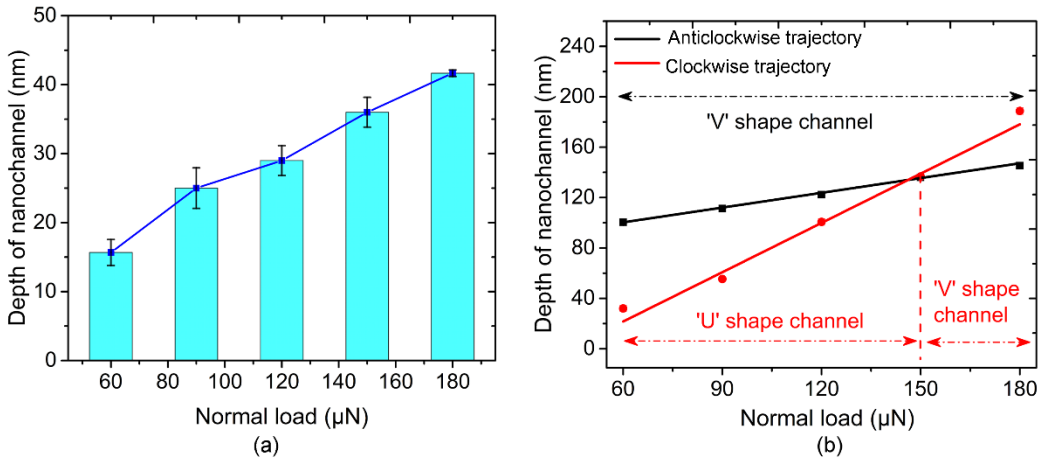

Fig. 4. Relationship between the nanochannel depth and the applied normal load. (a)

12

Fabrication with a single scratch. (b) Nanomilling with anticlockwise and clockwise trajectories.

Figure 5(a–c) shows schematic diagrams of the tip-edge trajectories when fabricated with a single scratch, and with anticlockwise and clockwise trajectories, respectively. Previous studies have demonstrated that the removal mechanisms of materials are determined by the attack angle (α) between the tip and sample surface [25,13]. Three removal mechanisms — plowing, wedge formation, and cutting — have been proposed to increase the attack angle [26]. Cutting is considered to be the dominant mechanism for material removal when the attack angle exceeds a critical value, which is approximately 70° [25,13]. As shown in Fig. 5(a), the attack angles for the left (α_1) and right (α_2) cutting edge were approximately 120° and 60°, respectively, which results in material being removed by cutting and chip formation. Hence, there was almost no pile-up on either side of the channel (Fig. 3(a)).

For the nanomilling process, the channel morphology mainly depended on the edge of the tip trajectory. Figure 5(b) illustrates the tip-edge trajectory in one anticlockwise nanomilling period. The enlarged images are of the area marked in the red dashed rectangle. The left attack angle (α_3) was far smaller than the critical value for cutting (~70°). Thus, the materials were expelled by ploughing and accumulated on the side of the machined nanochannel, resulting in pile-ups on the left side of the tip feed direction (Fig. 3(b)). However, the right attack angle (α_4) was relatively close to the critical value for the cutting mode. In this case, the materials were removed by cutting and no pile-up can be found at the right side of the tip feed direction (Fig. 3(b)). The undeformed chip thickness during nanomilling reached the nanometer

scale, which is comparable with the radius of the tip edge. According to the reports of Fang et al. [27,28], in contrast with conventional micro-cutting, material removal for nanoscale-cutting occurs by extrusion rather than by a shearing mechanism. Thus, in the cutting mode of the nanomilling process, materials were expelled by extrusion. The tip-edge trajectory in one clockwise nanomilling period is depicted in Fig. 5(c), where the enlarged schematic shows the region marked in red dashed rectangle. As was the case for anticlockwise nanomilling, pile-ups were generated on the left side of the tip feed direction (Fig. 3(c) and (d)) owing to the small attack angle (α_5).

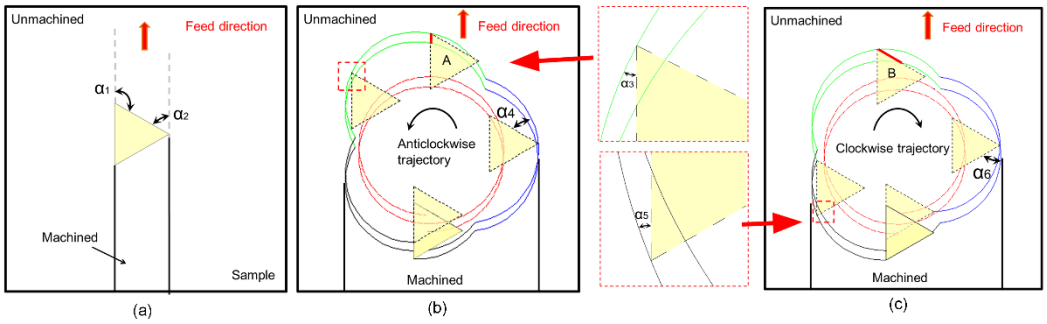

Fig. 5. (a–c) Schematic diagrams of the tip-edge trajectories when fabricated using a single scratch, and with anticlockwise and clockwise trajectories, respectively.

To better understand the material-removal process during nanomilling, the displacement vectors of the silicon atoms in a nanomilling period were revealed using MD simulations. Figure 6 shows snapshots of the atomic flow fields in the workpieces when the tip rotates in one period with the anticlockwise trajectory. As depicted in Fig. 6(a), the tip moves from position IV to I and the atomic flows mainly moves in the $[\bar{1}\bar{2}0]$ and $[0\bar{1}0]$ directions because of the material extrusion by the tip. When the tip moves from position I to II (Fig. 6(b)), the atoms adjacent to the edge 'AB' move in the $[5\bar{1}0]$ direction because of the elastic recovery of the specimen. Atoms

14

near the edge 'BC' move in the $[5\bar{1}0]$ and $[1\bar{3}0]$ directions, which contributes to the formation of pile-up on the left side of the tip feed direction. Figure 6(c) and (d) illustrate the atomic flows for the tip moving from position II to III and III to IV, respectively. In Fig. 6(c), the atoms move in the $[\bar{2}30]$ and $[\bar{1}30]$ directions. In Fig. 6(d), the atoms are pushed forward in the $[\bar{5}10]$ and $[\bar{4}\bar{1}0]$ directions by the edge 'AB', which leads to chip formation. Furthermore, the atoms flowing in the $[\bar{6}10]$ direction contribute to the generation of pile-ups.

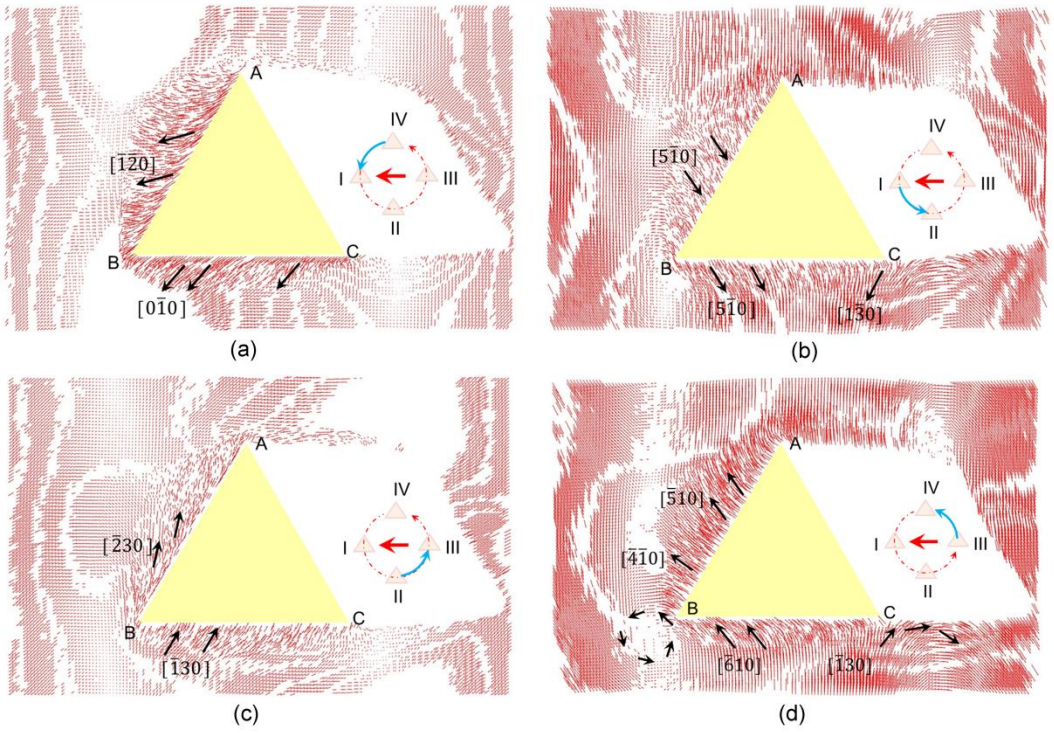

Fig. 6. (a–d) Snapshots of the atomic flow fields in the workpieces when tip moves from position IV to I, I to II, II to III, and III to IV, respectively.

The machined depth of the nanochannel is inversely proportional to the horizontal projection of the contact area between the tip and sample when the applied normal load is constant [29]. The red lines in Fig. 5(b) and (c) represent the contact area between the tip and sample when the tip is at positions A and B, respectively. The contact area for the clockwise trajectory is larger than for the anticlockwise

trajectory. Thus, depth of the nanochannel fabricated using a clockwise trajectory is smaller than that machined by anticlockwise trajectory when the normal load is smaller than 150 μN (Fig. 4(b)).

Using the method proposed by Varenberg et al, the horizontal force in the nanomilling process was calibrated and measured [30,31]. Figure 7(a) shows the recorded experimental horizontal forces for anticlockwise and clockwise nanomilling with a normal load of 180 μN. The horizontal force is smaller for clockwise nanomilling than for anticlockwise nanomilling. Figure 7(b) illustrates the horizontal force obtained from MD simulations for machining with an anticlockwise trajectory. The force becomes stable after machining for a distance of approximately 11.5 nm. The tip torsion during machining is proportional to the horizontal force [30]. A large tip torsion due to a large horizontal force enlarges the contact area between the tip and sample. Hence, for a normal load of 180 μN, the nanochannel depth was greater under clockwise than anticlockwise milling. A schematic diagram of the nanomilling process is shown in Fig. 7(c). Because the applied normal load is constant in nanomilling, the tip can scratch the specimen at all times. The real tip trajectory for anticlockwise nanomilling is depicted as Fig. 7(d), which is an inclined ellipse in space. As shown in the side view of Fig. 7(d), the inclined ellipse trajectory contributes to the ‘V’ shape of nanochannels fabricated using the anticlockwise trajectory. For nanomilling with a clockwise trajectory (Fig. 7(e)), the real tip trajectory is closer to a circle than to an inclined ellipse owing to the shallower machined depth at applied normal loads smaller than 150 μN. The machined

16

nanochannels display a ‘U’ shape in this case. However, when the normal load exceeds 150 μN, because of the large machined depth, the real tip trajectory approaches an inclined ellipse trajectory similar to that for anticlockwise nanomilling. Hence, a ‘V’-shaped nanochannel is obtained.

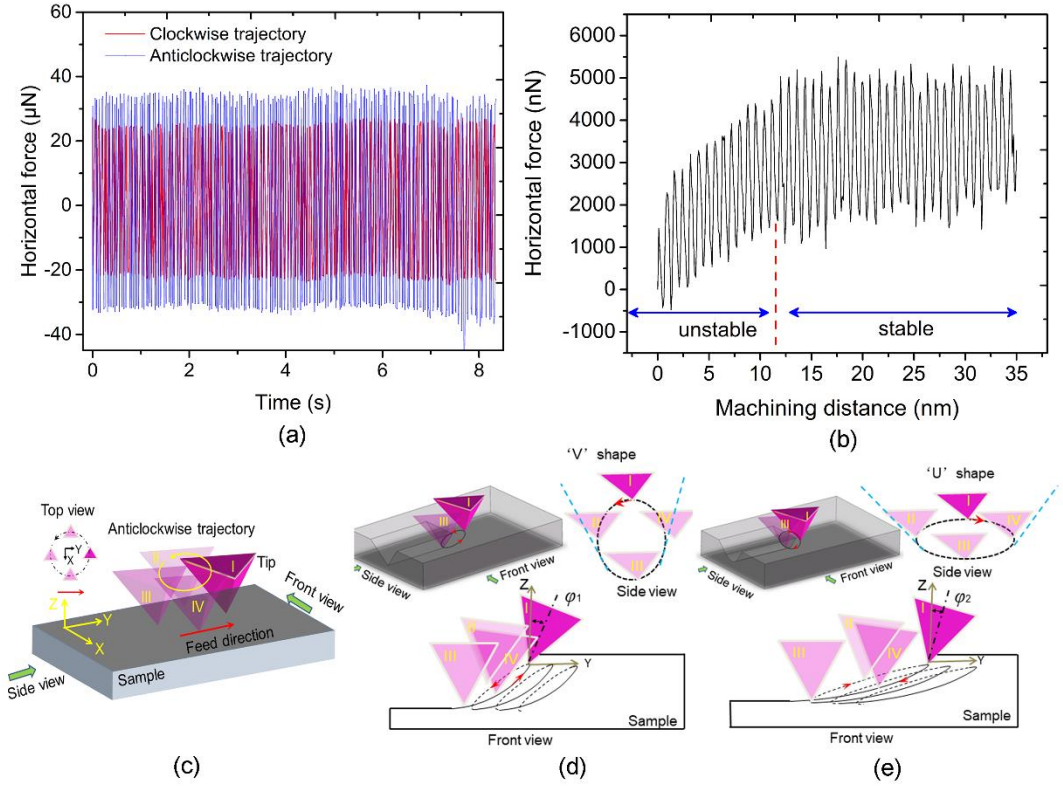

Fig. 7. (a) Experimental horizontal forces recorded for anticlockwise and clockwise trajectories with a normal load of 180 μN. (b) MD-simulated horizontal force for the anticlockwise trajectory. (c–e) Schematic diagrams of the nanomilling process, and the anticlockwise and clockwise nanomilling trajectories, respectively.

To further reveal the influence of the trajectory shape on the processing outcomes, as shown in Fig. 8(a), the acronym of ‘tib-based nanomilling’, which includes curved trajectories, was fabricated using clockwise nanomilling. A circle (indicated by I in Fig. 8(a)) machined by the circle trajectory can be observed. Fig. 8(b) shows the

17

cross-sections corresponding to the curved channels in Fig. 8(a). It is obvious that the curved channels demonstrate a 'U' shape, which is constant with the result of the aforementioned clockwise nanomilling. Furthermore, from the cross-section II-II', one can see that the pile-ups almost distribute uniformly on both sides of the channel. However, the pile-ups mainly distribute on the left side of the channel for the cross-section III-III'. The variation of the feed direction during nanomilling the curved channel contributes to the variation of the pile-ups.

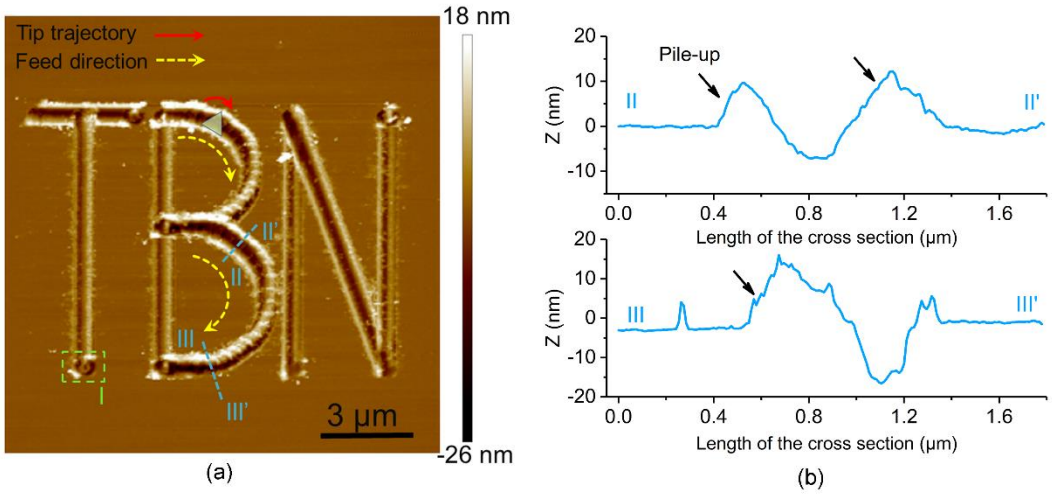

Fig. 8. (a) AFM image of TBN fabricated using nanomilling approach. The 'TBN' is the acronym of tib-based nanomilling. (b) Cross-section of the channels that marked in (a).

3.2 Phase transformation

Mechanical machining induces a series of phase transformations in single-crystal silicon because the hydrostatic pressure exceeds the pressure limit [32,33]. Specifically, a new phase, labeled Si-II, forms under the tip. This phase transforms from Si-I and is not stable at ambient pressure [33, 34]. The Si-II phase further transforms during unloading depending on the pressure release rate, transforming into α-Si at high unloading rates, and into Si-III and Si-XII at low unloading rates [35]. We

performed Raman spectroscopy on a rectangular area (10 μm × 7 μm) with a depth of 120 nm that was machined using nanomilling. The Raman spectrum from the nanomilling region indicated in Fig. 9(a) is shown in Fig. 9(b); a spectrum for a pristine sample is provided for comparison. Three characteristic peaks (150, 470, and 521 cm^{-1}) of the nanomilling spectrum can be observed. We identify the sharp peak at 521 cm^{-1} as the Si-I phase, and the two broadband peaks at 150 and 470 cm^{-1} as the α-Si phase [36]. Thus, the α-Si phase is induced under the high unloading rate of the nanomilling process.

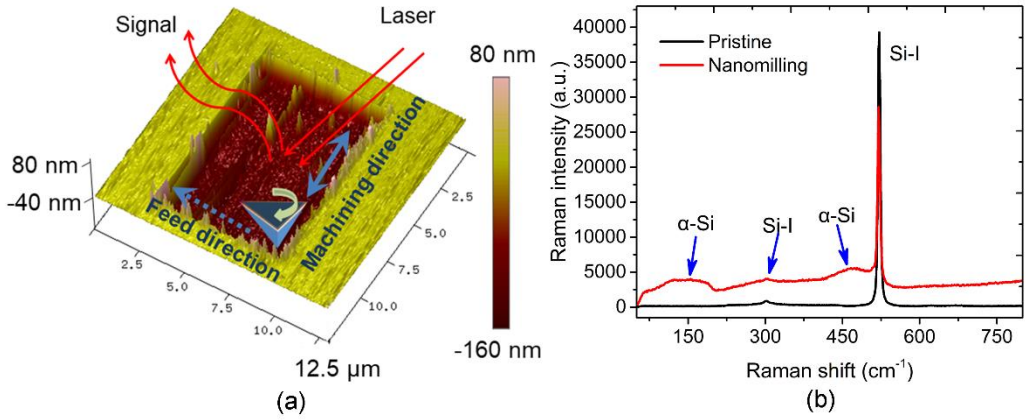

Fig. 9. (a) Annotated AFM image illustrating the process of Raman detection. (b) Raman spectra acquired from the nanomilling region and of a pristine sample.

We carried out MD simulations to further investigate the phase transformation of the single-crystal silicon during nanomilling. The evolution of the crystalline phases is consistent with the distribution of the hydrostatic stress [37,38]. The hydrostatic stress can be calculated using a method proposed by Goel et al. [39]. Figure 10(a) and (b) show the hydrostatic stress distributions when machining at positions I and III. High-pressure zones can be observed in front of the tip (areas a_1 and b_1) and beneath the tip (areas a_2 and b_2). The sample undergoes a phase transformation from Si-I to Si-II

19

under high pressure, which contributes to plastic deformation in these zones. The tip extrudes the sample material more severely at position I than position II, which leads to a larger hydrostatic stress zone in area a_1. The coordination numbers (n) in the workpiece were used to identify the different phases forms, such as the diamond crystal phase, bct-silicon, and β-silicon.

Figure 10(c) and (d) show the cross-sections of the phase transformation of the single silicon atoms corresponding to the hydrostatic stress distributions shown in Fig. 10(a) and (b). The pile-up indicated by the black rectangle (area c_1) in Fig. 10(c) includes bct-silicon (n = 5). Furthermore, the regions in front of the tip (area c_2) and under the tip (area c_3), which are indicated by the red and gray rectangles, respectively, are composed of amorphous silicon atoms mixed with bct-silicon (n = 5), β-silicon (n = 6), and metastable atoms (n = 7). When the tip moves back to position III, as illustrated in Fig. 10(d), the number of bct-silicon atoms in the pile-ups and the tip – sample contact area (area d_1) become smaller than at position I because of the uploading process. However, there are more metastable atoms in the region under the tip (area d_2) than in area c_3, as shown in Fig. 10(c).

Based on these simulation results, the phase transformation during nanomilling can be described as follows. At position I, owing to the effect of tip extrusion, the atoms in the contact area between the tip and sample (area c_2) transform from diamond cubic four-coordinated α-silicon to bct-silicon, β-silicon, and metastable atoms. The pile-up is generated by the extrusion and is mainly composed of bct-silicon. The diamond cubic four-coordinated α-silicon atoms under the tip (area c_3)

also transform to bct-silicon, β-silicon, and metastable atoms, which induces subsurface damage. As the tip passes and moves to position III, the stress of the silicon atoms in front of the tip is released and the number of bct-silicon atoms decreases. However, more metastable atoms (n = 7) are generated by the pressing of the tip in area c_2, which further contributes to the subsurface damage. The final subsurface of the nanochannel is shown in the enlarged image of area d_3 in Fig. 10(d), which includes bct-silicon (n = 5) and several β-silicon atoms.

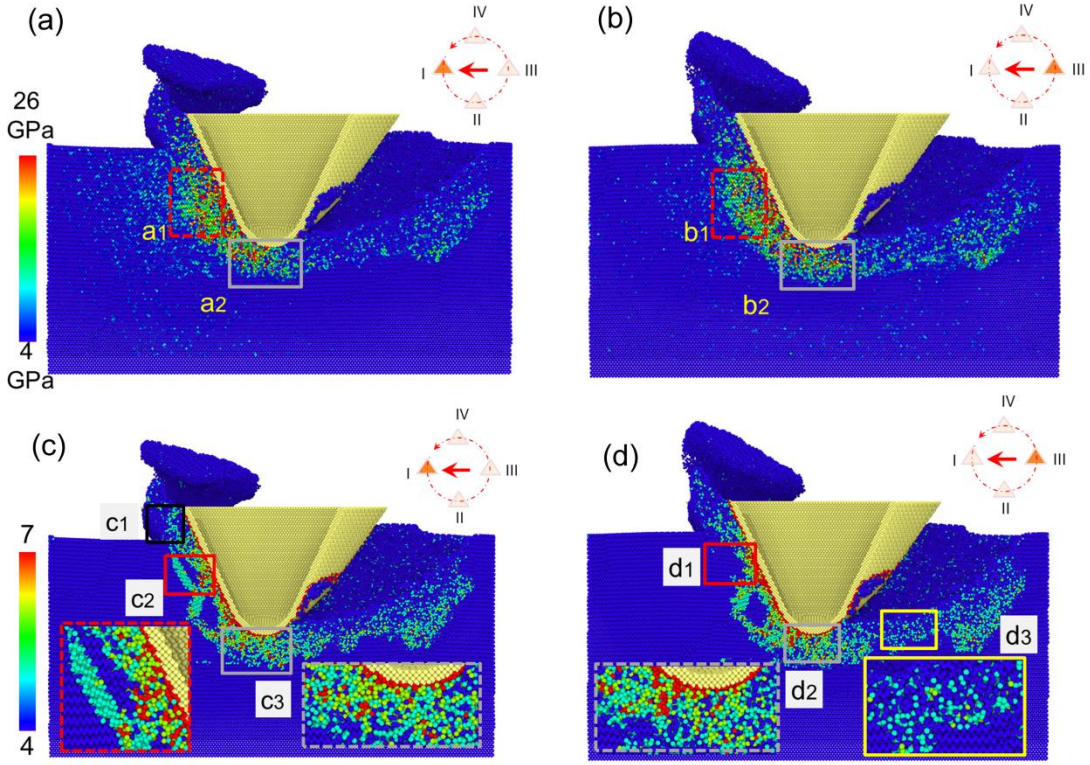

Fig. 10. (a,b) Stress distributions at points I and III, respectively, of the nanochannel. (c,d) Phase transformation at points I and III, respectively, of the nanochannel simulated via MD.

3.3 Subsurface damage

The subsurface of the nanochannel fabricated with a circular trajectory was investigated using TEM. As shown in Fig. 11(a), a protective Pt layer was deposited on the nanochannel surface during the preparation of the TEM sample to avoid the

21

subsurface damage caused by the FIB. A grey layer beneath the Pt protective layer can be observed in Fig. 11(a), which was identify as α-Si [36,40]. This observation agrees with the Raman results. The maximum depth (*D*) of the distorted Si-I region is approximately 150 nm. The enlarged image (Fig. 11(b)) of the region 1 marked in Fig. 11(a) shows that there are no atomic defects in the area far from the distorted region. Furthermore, the diffraction pattern (Fig. 11(c)) corresponding to the area is indicative of a single crystal structure [41]. Thus, these results indicate the pristine sample material is a singe crystal without defects before machining. High-resolution TEM (HRTEM) was used to better understand the subsurface damage of the nanochannel. A region adjacent to the α-Si layer (indicated as 2 in Fig. 11(a)) was selected. As shown in Fig. 11(d), it is evident that dislocations and stacking faults were induced in the adjacent area between the α-Si layer and the distorted Si-I region. Figure 11(e) demonstrates the HRTEM image of region 3 in Fig. 11(a). Dislocations and stacking faults also can be observed. These atomic-scale defects are generated by the high pressure and shear stress during nanomilling [42]. Wu et al conducted nanoscratching on monocrystalline silicon using a diamond tip and only α-Si, dislocations, and stacking faults were observed in the subsurface [43], which indicates the subsurface damages are almost identical for nanoscratching and nanomilling.

22

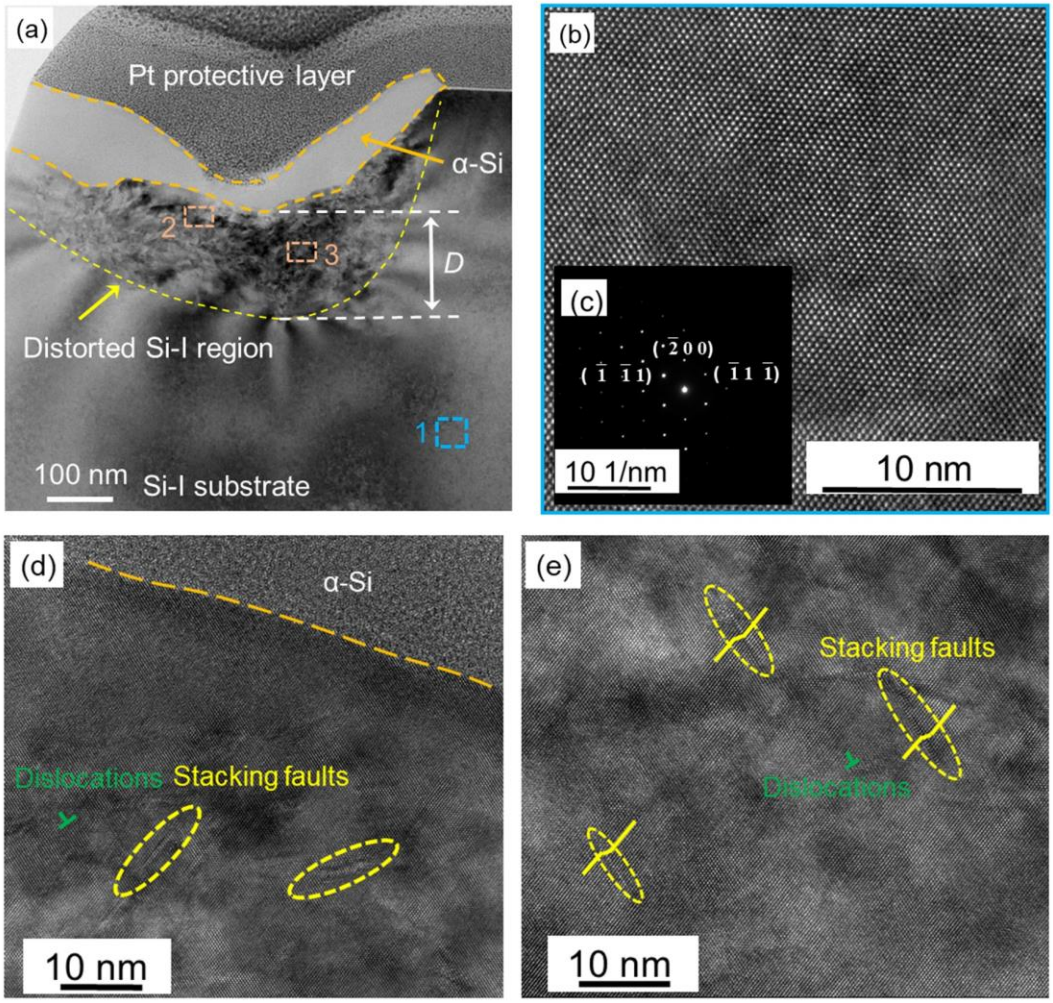

Fig. 11. (a) TEM image of the subsurface of the cross-section for a nanochannel machined by nanomilling with circular trajectory. (b,c) HRTEM image and diffraction of the region 1 marked in (a), respectively. (d,e) HRTEM images of the regions 2 and 3 that marked in (a), respectively.

We summarized the dislocation networks generated by anticlockwise and clockwise nanomilling trajectories using dislocation analysis based on MD simulations. As shown in Figs. 12(a) and (b), dislocations and their Burgers vectors were identified using the dislocation extraction algorithm, where the Burgers vectors 1/2 [110], 1/6 [112], and unidentified dislocations are colored blue, green, and red, respectively. For anticlockwise nanomilling (Fig. 12(a)), the dislocation loops with Burgers vector 1/2 [110] were distributed in front of the tip because of the extrusion

23

of the tip. For clockwise nanomilling (Fig. 12(b)), dislocations with Burgers vector 1/2[110] also formed in front of the tip. However, the length of these dislocations was much smaller than that generated in anticlockwise nanomilling. Furthermore, more dislocations were generated on the right side of the nanochannel. The full length of the induced dislocations for anticlockwise and clockwise nanomilling were 263 nm and 204 nm, respectively, which indicates anticlockwise nanomilling contributing to longer dislocations compared with clockwise nanomilling. Figs. 12(c) and (d) illustrate the cross-section views of the nanochannel at the machining distance of 26 nm when nanomilling with an anticlockwise and a clockwise trajectory, respectively. It is observable that the depth of the subsurface damage (D_1) induced by anticlockwise nanomilling is much deeper than that induced by clockwise nanomilling (D_2). The MD simulation reveals the tip trajectory has a strong influence on the plastic deformation of the material. Furthermore, clockwise nanomilling could facilitate a shallower subsurface damage compared with anticlockwise nanomilling.

24

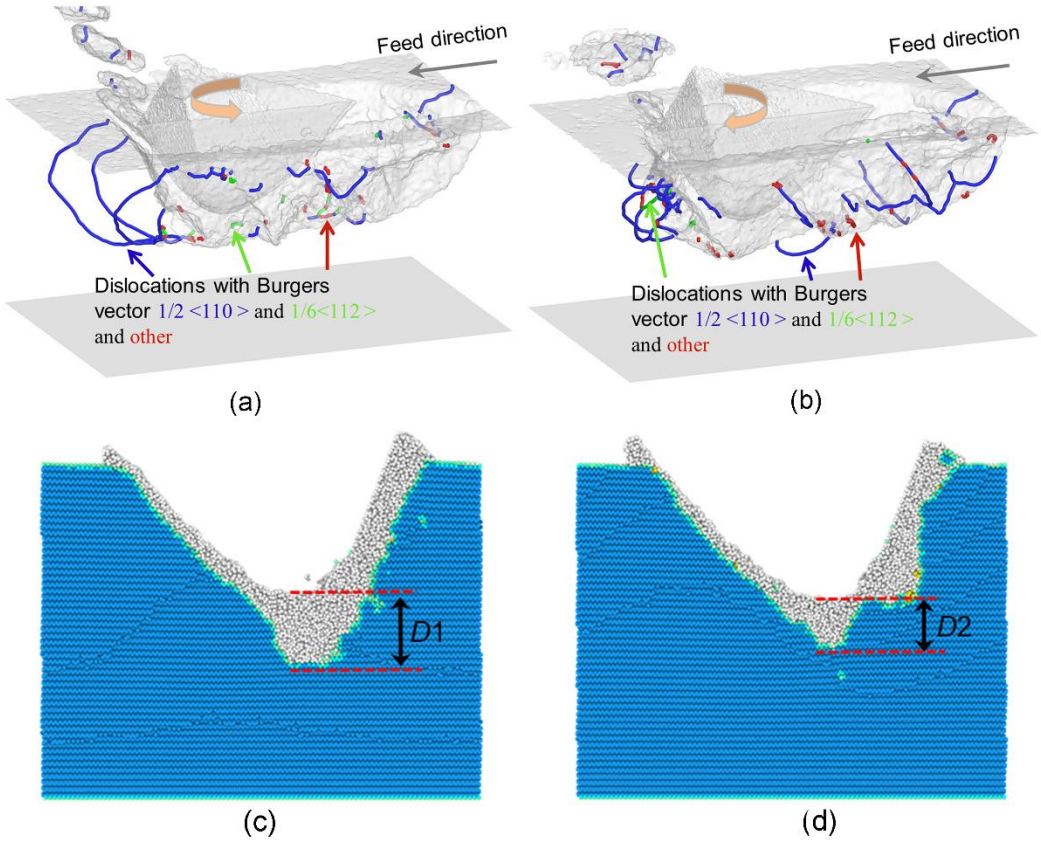

Fig. 12. Distribution of the dislocations obtained by MD simulations in single-crystal silicon for nanomillling with (a) an anticlockwise and (b) a clockwise trajectory. (c,d) The cross-section view of the nanochannel at the machining distance of 26 nm when nanomilling with an anticlockwise and a clockwise trajectory, respectively.

4. Conclusions

Using an AFM tip-based nanomilling set-up, nanochannels were fabricated on single-crystal silicon with a single scratch, and with anticlockwise and clockwise nanomilling trajectories. The morphology of the obtained nanochannels, phase transformations, and subsurface characteristics were investigated. The main findings are summarized as follows:

(1) Experimental observation and analysis of the atomic flow fields using MD simulations revealed that the channel shape depends on the tip trajectory and applied

25

normal load. For an anticlockwise nanomilling trajectory, the nanochannel had a 'V' shape at all loads. However, for normal loads smaller than 150 μN, the nanochannel fabricated using a clockwise nanomilling trajectory had a 'U' shape, which is caused by the real trajectory that is closer to a circle than to an inclined ellipse. The volume of material removed by nanomilling was about 10 times larger than that machined by a single scratch.

(2) The atomic structure of the fabricated nanostructures was investigated by Raman spectroscopy, which demonstrated that the α-Si phase was generated because of the high unloading rate. The dynamic evolution of phase transformation was revealed by MD simulations, which showed that the final subsurface of the nanochannel included bct-silicon and β-silicon atoms.

(3) TEM observations showed that many atomic-scale defects, such as dislocations and stacking faults, were induced in the subsurface of the nanochannels. MD simulations revealed that the length of the dislocations with Burgers vector 1/2 [110] was smaller for clockwise than anticlockwise nanomilling. In addition, more dislocations were generated on the right side of the channel for clockwise nanomilling.

Acknowledgements

The authors gratefully acknowledge the financial supports of the National Natural Science Foundation of China (51911530206, 52035004), Natural Science Foundation of Heilongjiang Province of China (YQ2020E015), Self-Planned Task (NO. SKLRS202001C) of State Key Laboratory of Robotics and System (HIT) and "Youth Talent Support Project" of the Chinese Association for Science and Technology.

References

[1] J. Yin, W. Gao, Z. Zhang, Y. Mai, A. Luan, H. Jin, J. Jian. Q. Jin, Batch microfabrication of highly integrated silicon-based electrochemical sensor and performance evaluation via nitrite water contaminant determination, Electrochimica Acta 335 (2020) 135660.

[2] J. Li, D. Geng, D. Zhang, W. Qin, Y. Jiang, Ultrasonic vibration mill-grinding of single-crystal silicon carbide for pressure sensor diaphragms, Ceramic International 44 (2018) 3107-3112.

[3] C. Jiang, Q. Liu, X. Wang, Direct investigation of methane nanofluidic microstructure and system dynamics in rough silicon nanochannel, Microfluidics and Nanofluidic 23 (2019) 120.

[4] F. Ebrahimi, L. Kalwani, Fracture anisotropy in silicon single crystal, Materials Science and Engineering: A 268 (1999) 116-126.

[5] C. Lauener, L. Petho, M. Chen, Y. Xiao, J. Michler, J. Wheeler, Fracture of silicon: influence of rate, positioning accuracy, FIB machining, and elevated temperatures on toughness measured by pillar indentation splitting, Materials & Design 142 (2018) 340-349.

[6] J. Zhang, J. Zhang, T. Cui, Z. Hao, A. Zahrani, Sculpturing of single crystal silicon microstructures by elliptical vibration cutting, Journal of Manufacturing Processes 29 (2017) 389-398.

[7] T. Zhang, Y. Zhao, T. Yu, T. Yu, J. Shi, J. Zhao, Study on polishing slurry waste reduction in polishing monocrystalline silicon based on ultrasonic atomization, Journal of Cleaner Production 233 (2019) 1-12.

[8] C. Li, X. Li, Y. Wu, F. Zhang. H. Huang, Deformation mechanism and force modelling of the grinding of YAG single crystals, International Journal of Machine Tools & Manufacture 143 (2019) 23-37.

[9] C. Li, F. Zhang, X. Wang, X. Rao, Repeated nanoscratch and double nanoscratch tests of Lu_2O_3 transparent ceramics: Material removal and deformation mechanism, and theoretical model of penetration depth, Journal of the European Ceramic Society 38 (2018) 705-718.

[10] Y. Yan, Y. Geng, Z. Hu, Recent advances in AFM tip-based nanomechanical machining, International Journal of Machine Tools & Manufacture 99 (2015) 1-18.

[11] Y. Yan, J. Wang, Y. Geng, Z. Fang, Y. He, Implementation of AFM tip-based nanoscratching process on single crystal copper: study of material removal state, Applied Surface Science 459

(2018) 723-731.

[12] H. Liu, P. Zhao, Y. Guo, D. Li, J. Wang, Material Removal Mechanism of FCC Single-crystalline Materials at nano-scales: Chip Removal and Ploughing, Journal of Materials Processing Technology 294 (2021) 117106.

[13] Y. Geng, Y. Yan, Y. Xing, X. Zhao, Z. Hu, Modelling and experimental study of machined depth in AFM-based milling of nanochannels, International Journal of Machine Tools & Manufacture 73 (2013) 87-96.

[14] J. Wang, Y. Yan, Y. Geng, Y. Gan, Z. Fang, Fabrication of polydimethylsiloxane nanofluidic chips under AFM tip-based nanomilling process, Nanoscale Research Letters 14 (2019) 136.

[15] B. Gozen, O. Ozdoganlar, A Rotating-tip-based mechanical nano-manufacturing process: nanomilling, Nanoscale Research Letters 5 (2010) 1403-1407.

[16] L. Zhang, J. Dong, P. Cohen. Material-insensitive feature depth control and machining force reduction by ultrasonic vibration in AFM-based nanomachining, IEEE Transactions on Nanotechnology 12 (2013) 743-750.

[17] S. Park, M. Mostofa, C. Park, M. Mehrpouya, S. Kim, Vibration assisted nano mechanical machining using AFM prob. CIRP Annals-Manufacturing Technology 63 (2014) 537-540.

[18] H. Li, T. Yu, L. Zhu, W. Wang, Analytical modeling of grinding-induced subsurface damage in monocrystalline silicon, Materials & Design 130 (2017) 250-262.

[19] J. Wang, Y. Yan, Z. Li, Y. Geng, Towards understanding the machining mechanism of the atomic force microscopy tip-based nanomilling process, International Journal of Machine Tools & Manufacture 162 (2021) 103701.

[20] J. Sun, L. Chen, J. Han, A. Ma, L. Fang, Nanoindentation induced deformation and pop-in events in a silicon crystal: molecular dynamics simulation and experiment, Scientific reports 7 (2017) 10282.

[21] S. Goel, X. Luo, A. Agrawal, R. Reuben, Diamond machining of silicon: a review of advances in molecular dynamics simulation, International Journal of Machine Tools & Manufacture 88 (2015) 131-164.

[22] Q. Tang, MD simulation of dislocation mobility during cutting with diamond tip on silicon, Materials Science in Semiconductor Processing 10 (2007) 270-275.

[23] S. Plimpton, Fast parallel algorithms for short-range molecular dynamic, Journal of Computational Physics 117 (1995) 1-19.

[24] A. Stukowski, Visualization and analysis of atomistic simulation data with OVITO-the Open Visualization Tool, Modeling and Simulation in Materials Science and Engineering 18 (2010) 015012.

[25] V. Koinkar, B. Bhushan, Scanning and transmission electron microscopies of single-crystal silicon microworn/machined using atomic force microscopy, Journal of Materials Research 12 (1997) 3219-3224.

[26] K. Hokkirigawa, K. Kato, An experimental and theoretical investigation of plowing, cutting and wedge formation during abrasive wear, Tribology International 21 (1988) 51-57.

[27] F. Fang, H. Wu, Y. Liu, Modelling and experimental investigation on nanometric cutting of monocrystalline silicon, International Journal of Machine Tools & Manufacture 4 (2005) 1681-1686.

[28] F. Fang, H. Wu, W. Zhou, X. Hu, A study on mechanism of nano-cutting single crystal silicon, Journal of Materials Processing Technology 184 (2007) 407-410.

[29] F. Zhang, B. Meng, Y. Geng, Y. Zhang, Study on the machined depth when nanoscratching on 6H-SiC usingBerkovich indenter: Modelling and experimental study, Applied Surface Science 368 (2016) 449-455.

[30] J. Wang, Y. Yan, S. Chang, T. Wang, Y. Geng, Y. Gan, Study of the formation mechanism of bundle structures using AFM tip-based nanoscratching approach. Tribology International 142 (2020) 106000.

[31] M. Varenberg, I. Etsion, G. Haiperin. An improved wedge calibration method for lateral force in atomic force microscopy, Review of Scientific Instruments 74 (2003) 3362.

[32] Y. Wu, H. Huang, J. Zou, L. Zhang, J. Delld, Nanoscratch-induced phase transformation of monocrystalline Si, Scripta Materialia 63 (2010) 847-850.

[33] D. Ge, V. Domnich, Y. Gogotsi, High-resolution transmission electron microscopy study of metastable silicon phases produced by nanoindentation, Journal of Applied Physics 93 (2003) 2418.

[34] D. Callahan, J. Morris, The Extent of Phase-transformation in Silicon Hardness Indentations,

Journal of Materials Research 7 (1992) 1614-1617.

[35] G. Gassilloud, C. Ballif, P. Gasser, G. Buerki, J. Michler, Deformation mechanisms of silicon during nanoscratching, Physica Status Solidi A-Applications and Materials Science 202 (2005) 2858-2869.

[36] J. Yan, T. Asami, H. Harada, T. Kuriyagawa, Fundamental investigation of subsurface damage in single crystalline silicon caused by diamond machining, Precision Engineering 33 (2009) 378-386.

[37] K. Mylvaganam, L. Zhang, P. Eyben, J. Mody, W. Vandervorst, Evolution of metastable phases in silicon during nanoindentation: mechanism analysis and experimental verification, Nanotechnology 20 (2009) 305705.

[38] H. Dai, S. Li, G. Chen, Molecular dynamics simulation of subsurface damage mechanism during nanoscratching of single crystal silicon, Proceedings of the institution of Mechanical Engineers Part J-Journal of Engineering Tribology 233 (2019) 61-73.

[39] S. Goel, X. Luo, R. Reuben, Wear mechanism of diamond tools against single crystal silicon in single point diamond turning process, Tribology International 57 (2013) 272-281.

[40] L. Wu, B. Yu, P. Zhang, C. Feng, P. Chen, L. Deng, J. Gao, S. Chen, S. Jiang, L. Qian, Rapid identification of ultrathin amorphous damage on monocrystalline silicon surface, Physical Chemistry Chemical Physics 22 (2020) 12987.

[41] X. Rao, F. Zhang, Y. Lu, X. Luo, F. Chen, Surface and subsurface damage of reaction-bonded silicon carbide induced by electrical discharge diamond grinding, International Journal of Machine Tools and Manufacture 154 (2020) 103564.

[42] A. Minor, E. Lilleodden, M. Jin, E. Stach, D. Chrzan, J. Morris, Room temperature dislocation plasticity in silicon, Philosophical Magazine 85 (2005) 323-330.

[43] Y. Wu, H. Huang, J. Zou, Deformation of monocrystalline silicon under nanoscratching, Advanced Materials Research 41-42 (2008) 15-19.